Tectono-thermal Evolution of a Distal Rifted Margin: Constraints From the Calizzano Massif (Prepiedmont-Briançonnais Domain, Ligurian Alps)

Alessandro Decarlis, Maria Giuditta Fellin, Matteo Maino, Simona Ferrando, Gianreto Manatschal, Laura Gaggero, Silvio Seno, Finlay M Stuart, Marco Beltrando

AGU PUBLICATIONS

Tectonics

RESEARCH ARTICLE
10.1002/2017TC004634

Special Section:
Orogenic Cycles: From Field Observations to Global Geodynamics

Tectono-thermal Evolution of a Distal Rifted Margin: Constraints From the Calizzano Massif (Prepiedmont-Briançonnais Domain, Ligurian Alps)

Alessandro Decarlis[1,2], Maria Giuditta Fellin[3], Matteo Maino[4], Simona Ferrando[1], Gianreto Manatschal[2], Laura Gaggero[5], Silvio Seno[4], Finlay M. Stuart[6], and Marco Beltrando[1]

[1]Dipartimento di Scienze della Terra, Università degli Studi di Torino, Turin, Italy, [2]EOST, IPGS, Universitè de Strasbourg, Strasbourg CEDEX, France, [3]Department of Earth sciences, ETH Zurich, Zurich, Switzerland, [4]Dipartimento di Scienze della Terra e dell'Ambiente, Università degli Studi di Pavia, Pavia, Italy, [5]Dipartimento di Scienza della Terra dell'Ambiente e della Vita, Università di Genova, Genoa, Italy, [6]Isotope Geosciences Unit, SUERC, East Kilbride, UK

Abstract The thermal evolution of distal domains along rifted margins is at present poorly constrained. In this study, we show that a thermal pulse, most likely triggered by lithospheric thinning and asthenospheric rise, is recorded at upper crustal levels and may also influence the diagenetic processes in the overlying sediments, thus representing a critical aspect for the evaluation of hydrocarbon systems. The thermal history of a distal sector of the Alpine Tethys rifted margin preserved in the Ligurian Alps (Case Tuberto-Calizzano unit) is investigated with thermochronological methods and petrologic observations. The studied unit is composed of a polymetamorphic basement and a sedimentary cover, providing a complete section through the prerift, synrift, and postrift system. Zircon fission track analyses on basement rocks samples suggest that temperatures exceeding ~240 ± 25°C were reached before ~150–160 Ma (Upper Jurassic) at few kilometer depth. Neoformation of green biotite, stable at temperatures of ~350 to 450°C, was synkinematic with this event. The tectonic setting of the studied unit suggests that the heating-cooling cycle took place during the formation of the distal rifted margin and terminated during Late Jurassic (150–160 Ma). Major crustal and lithospheric thinning likely promoted high geothermal gradients (~60–90°C/km) and triggered the circulation of hot, deep-seated fluids along brittle faults, causing the observed thermal anomaly. Our results suggest that rifting can generate thermal perturbations at relatively high temperatures (between ~240 and 450°C) at less than 3 km depth in the distal domains during major crustal thinning preceding breakup and onset of seafloor spreading.

Key Points:
- Distal rifted margins of magma-poor systems suffer a synrift thermal pulse
- The thermal anomaly at distal rifted margin also affects shallow crustal levels with relatively high temperatures of up to 350–450°
- The thermal anomaly is vehiculated toward the upper crust by hydrothermal activity concentrated along distal margin normal faults

Supporting Information:
- Supporting Information S1

Correspondence to:
A. Decarlis,
aledec@tin.it

Citation:
Decarlis, A., Fellin, M. G., Maino, M., Ferrando, S., Manatschal, G., Gaggero, L., … Beltrando, M. (2017). Tectono-thermal evolution of a distal rifted margin: Constraints from the Calizzano massif (Prepiedmont-Briançonnais domain, Ligurian Alps). *Tectonics*, *36*, 3209–3228. https://doi.org/10.1002/2017TC004634

Received 19 APR 2017
Accepted 14 NOV 2017
Accepted article online 27 NOV 2017
Published online 22 DEC 2017

1. Introduction

The tectonic evolution of rift systems is characterized by markedly different dynamics occurring at proximal and distal margins (e.g., Sutra et al., 2013; Tugend et al., 2014, cum ref.). The passage from unthinned to thinned crustal domains marks a major change in timing and modality of the rift style across rifted margins (see Mohn et al., 2012, cum ref). The process of rift localization leads to the quiescence of tectonically active areas placed over thick continental crust in the proximal parts of the margins and to the activation of narrow sectors in which the crust becomes severely thinned (i.e., future distal margins). During final rifting, the deformation between lower and upper crust becomes "coupled" (see Sutra et al., 2013), generating new fluid circulation patterns (Incerpi et al., 2017). The circulation of hydrothermal fluids is typically associated with anomalous thermal gradients that lead to characteristic synrift heating/cooling cycles affecting the whole crustal section in the distal margin (Beltrando et al., 2015; Seymour et al., 2016). Remnants of fossil rifted margins, exposed inside orogenic belts, may provide an opportunity to directly investigate and evaluate the character of synrift heating events in the case the synorogenic metamorphism never exceed the maximum temperatures reached during rifting.

In this study we use two thermochronometric systems, zircon fission tracks (ZFTs) and zircon (U-Th)/He (ZHe), to investigate the synrift heating-cooling cycle at the distal rifted margin of the Alpine Tethys, which is one of the world's best fossil analogues for a magma-poor rifted margin (e.g., Decarlis et al., 2015; Haupert et al., 2016; Manatschal, 2004; Manatschal & Bernoulli, 1999; Mohn et al., 2012). Here we report new data that enable documentation of the thermal history of the Case Tuberto-Calizzano unit in the Ligurian Alps (Figure 1), which belong to the distal European margin of the Alpine Tethys system (Decarlis et al., 2013,

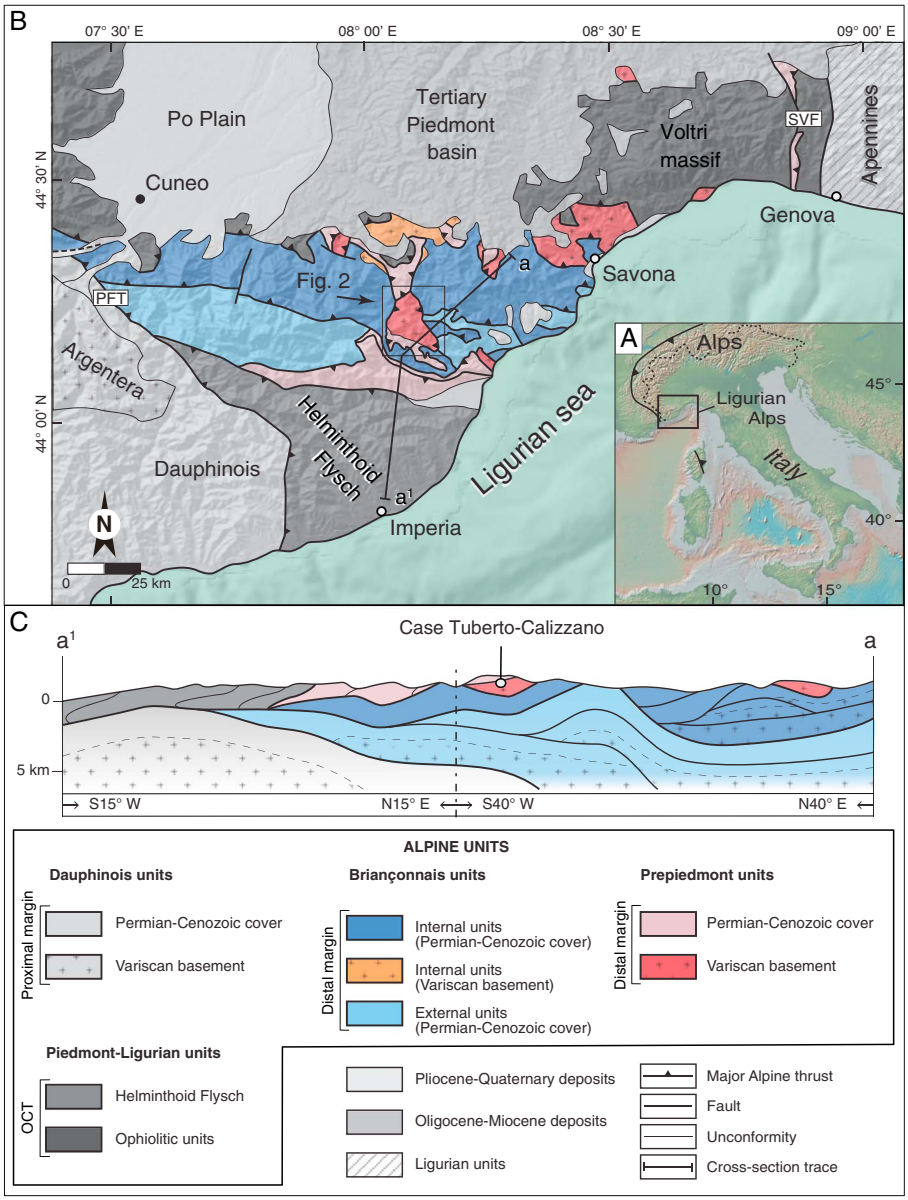

Figure 1. (a) Location and (b) structural map of the Ligurian Alps, from Vanossi (1991), modified. The box indicates location of the Case Tuberto-Calizzano unit, details in the related geological map of Figure 2. (c) Structural section through the Ligurian Alps, illustrating the position of the study area in the nappe pile, modified from Bonini et al. (2010).

2015). This unit only experienced low-grade Alpine metamorphism (Desmons et al., 1999; Seno et al., 2005a); thus, it offers a rare "window" into the thermal evolution of the ancient distal margin. The goal of this paper is to decipher the local temperature conditions reached in the basement during the thermal pulse and the time-window when it was active a few kilometers beneath synrift sediments.

2. Geological Setting

2.1. Alps Orogeny and Insights on Alpine Tethys Rift

The western and central sectors of the Alpine chain (Figure 1), which straddle the Italian, French, and Swiss borders, preserve the most indicative remnants of the Alpine Tethys rifted margins that survived the subsequent orogenic overprint. The Mesozoic Alpine rifting became active in the Early Jurassic (Froitzheim & Manatschal, 1996; Lemoine & Trümpy, 1987), leading to the separation of the European plate (north to

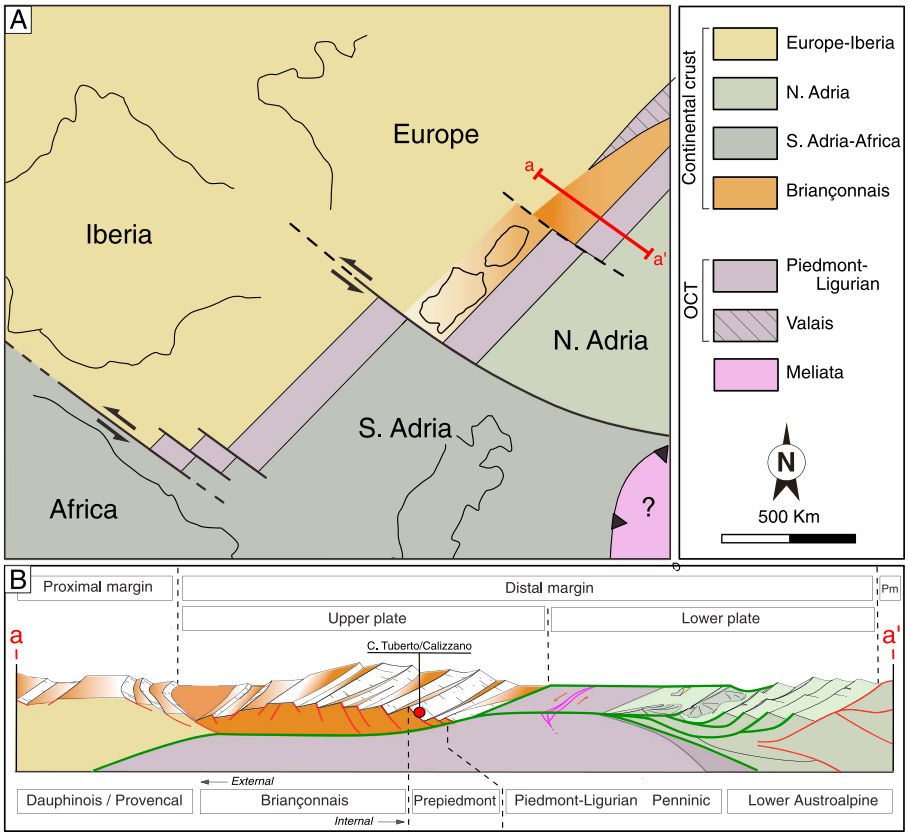

Figure 2. (a) Paleogeographic reconstruction of the Alpine Tethys during Late Jurassic (see Decarlis et al., 2017). (b) Simplified cross section across the Alpine Tethys illustrating the main Alpine paleogeographic structural domains and rifting domains (from Decarlis et al., 2015) (detachment faults in green).

north-west) from the Adria microplate (south to south-west; formerly part of Africa; Figure 2) and to the formation of the Piedmont-Ligurian Ocean during Early Cretaceous (Handy et al., 2010, cum ref.). It followed the onset of convergence/subduction in Late Cretaceous and the continental collision during Tertiary times (see De Graciansky et al., 2011).

The tectono-sedimentary evolution of the Alpine Tethys margins has been discussed by several studies (e.g., Decarlis et al., 2015; Masini et al., 2013), suggesting that the Jurassic rifting was the result of polyphase tectonics including the following: (i) stretching phase (Hettangian-Sinemurian) leading to the formation of widely distributed half-graben structures over only slightly extended 25 to 30 km thick continental crust, (ii) thinning phase (Pliensbachian-Toarcian) occurring only in a narrower area corresponding to the future distal margin, and (iii) hyperextension phase during which crustal and mantle rocks have been exhumed along detachment fault(s) at the seafloor.

During the final phase of hyperextension and exhumation, distal margins can be subdivided in upper plate (hanging wall of the exhumation system) and lower plate (Haupert et al., 2016; Decarlis et al., 2017; Figure 2). Stratigraphic and structural data reported by Lemoine et al. (1986), Decarlis et al. (2015), and Haupert et al. (2016) showed that in the present-day Alps, the Provençal, Dauphinois, and Upper Austroalpine units (Figure 2) represent remnants of the former proximal margins, whereas the internal European units and Lower Austroalpine units are derived from the former distal margin. At present, there is a general agreement that the internal European margin and the Austroalpine were the former upper and lower plate margin, respectively. The evolution of the upper plate is defined by a strong uplift and erosion on the Briançonnais margin, while the Prepiedmont (object of the present paper) and Piedmont domains were drowned. The Ligurian, Penninic, and Lower Austroalpine units represent the exhumed domain that was physically generated (exhumed) from Middle Jurassic onward.

2.2. Ligurian Alps

The Ligurian Alps are located at the southwestern end of the Western Alps arc, toward the transition with the Northern Apennine (Decarlis et al., 2014; Maino et al., 2013; Vanossi, 1991). They consist of a Variscan basement and of a Permian to Cenozoic sedimentary cover that were originally part of the paleo-European margin, belonging to the Briançonnais-Prepiedmont domains (Figures 1d and 2b). The Briançonnais domain was uplifted and eroded during rifting (Claudel & Dumont, 1999; Decarlis & Lualdi, 2008) as attested by a major synrift sedimentary hiatus. Conversely, the Prepiedmont domain displays a continuous clastic synrift sequence (Decarlis et al., 2015; Decarlis & Lualdi, 2011). From Late Cretaceous, as a consequence of the convergence and subsequent collision between the European and Adria plates, these rocks were buried and juxtaposed against remnants of exhumed subcontinental mantle, now exposed within the Voltri Massif (e.g., Bonini et al., 2010; Capponi & Crispini, 2002). The Briançonnais and Prepiedmont units experienced different Alpine metamorphic overprints (from anchizone to blueschist facies depending on their original position along the margin) (Desmons, Compagnoni et al., 1999; Desmons, Aprahamian et al., 1999; Messiga et al., 1981; Seno et al., 2005a), and since the Oligocene they were exhumed to upper crustal levels (Maino, Dallagiovanna, Dobson, et al., 2012; Seno et al., 2005a, 2005b).

The object of this study is the Case Tuberto-Calizzano unit that belongs to the Prepiedmont domain (Figure 2). It was treated in literature as a separate stack formed by the Case Tuberto unit (Permian and Mesozoic covers) (Dallagiovanna et al., 1984) and the Calizzano massif (basement unit) (Airoldi, 1937) until local evidence for stratigraphic continuity was reported by Dallagiovanna (1988) and Cortesogno et al. (1998). This unit is interpreted as the more external of the whole Prepiedmont domain on the basis of both its position across the nappe pile and its stratigraphic content (Vanossi, 1991). In a general section across the former rifted margin (Figure 2), its location would correspond to the boundary between the uplifted Briançonnais domain and the submerged Prepiedmont domain.

2.3. Case Tuberto-Calizzano Unit: Stratigraphic Outline

The "Calizzano massif" rests on the highest structural levels within the Briançonnais nappe stack, bounded downward by a SW dipping tectonic contact (Dallagiovanna et al., 1984) (Figures 1c and 3). The massif preserves evidence of a protracted Palaeozoic evolution in the Gneiss-Amphibolite Complex (e.g., Gaggero et al., 2004), wherein Middle-Late Cambrian bimodal effusive tholeiitic and transitional basalts and acidic calc-alkaline volcanites associated with pelitic, psammitic, and arenitic sediments were intruded by Late Cambrian-Early Ordovician granitoids (commonly labeled "Orthogneiss 1"), which underwent Early Ordovician metamorphic reequilibration under eclogite (760°C, $>$1.7 GPa) to amphibolite (680°C, $>$1.1 GPa) facies conditions (e.g., Cortesogno et al., 1993; Desmons et al., 1999; Gaggero et al., 2004).

The subsequent intrusion of large granitic bodies ("Orthogneiss 2") and minor gabbros at ~470–460 Ma was then followed by a Variscan medium to low-P amphibolite facies (~600–650°C, 0.4–0.6 GPa) schistogenous event at ~330 Ma (Gaggero et al., 2004) and by a folding event with production of actinolite + chlorite, greenschist-facies mineral assemblage (actinolite + chlorite) along axial planes of open folds (Gaggero et al., 2004). In the study area and in similar basement units (Nucetto and Savona massifs), Lower Carboniferous-Early Permian (327–274 Ma) ^{40}Ar-^{39}Ar and Rb/Sr ages (Barbieri et al., 2003; Del Moro et al., 1982) and local occurrence of Permian lava flows resting directly on the lower Palaeozoic metamorphic basement (Dallagiovanna et al., 2009; Maino, Dallagiovanna, Gaggero, et al., 2012) demonstrate that this folding event was followed by exhumation to shallow crustal levels.

The basement is locally overlain by Middle Permian pyroclastites and tuffs (Melogno porphyroids formation: about 150 m), followed by the Upper Permian to Lower Triassic conglomerates and sandstones (Monte Pianosa Formation and Ponte di Nava Quartzite: about 150 m), and by Middle Triassic to Lower Jurassic carbonate rocks (San Salvatore Dolostone and Rocca Prione Formation, M. Arena Dolostone, Veravo Limestone, and Rocca Liverna Limestone, 250 m in thickness) (Vanossi, 1991). As reported by Dallagiovanna (1988), the Upper Permian to Triassic *p.p.* succession may be locally replaced by some tens of meters of polymictic breccias and conglomerates sampling the aforementioned lithologies (Monte Pennino Breccia) (Crozi, 1998).

The Triassic-Jurassic successions grade upward into a poorly dated sedimentary sequence, which is commonly ascribed to the Jurassic-Eocene (Scravaion schists) sedimentary cycle (Dallagiovanna & Seno, 1984; Vanossi, 1991. Notably, this Mesozoic and Cenozoic sedimentary succession has been mainly inferred

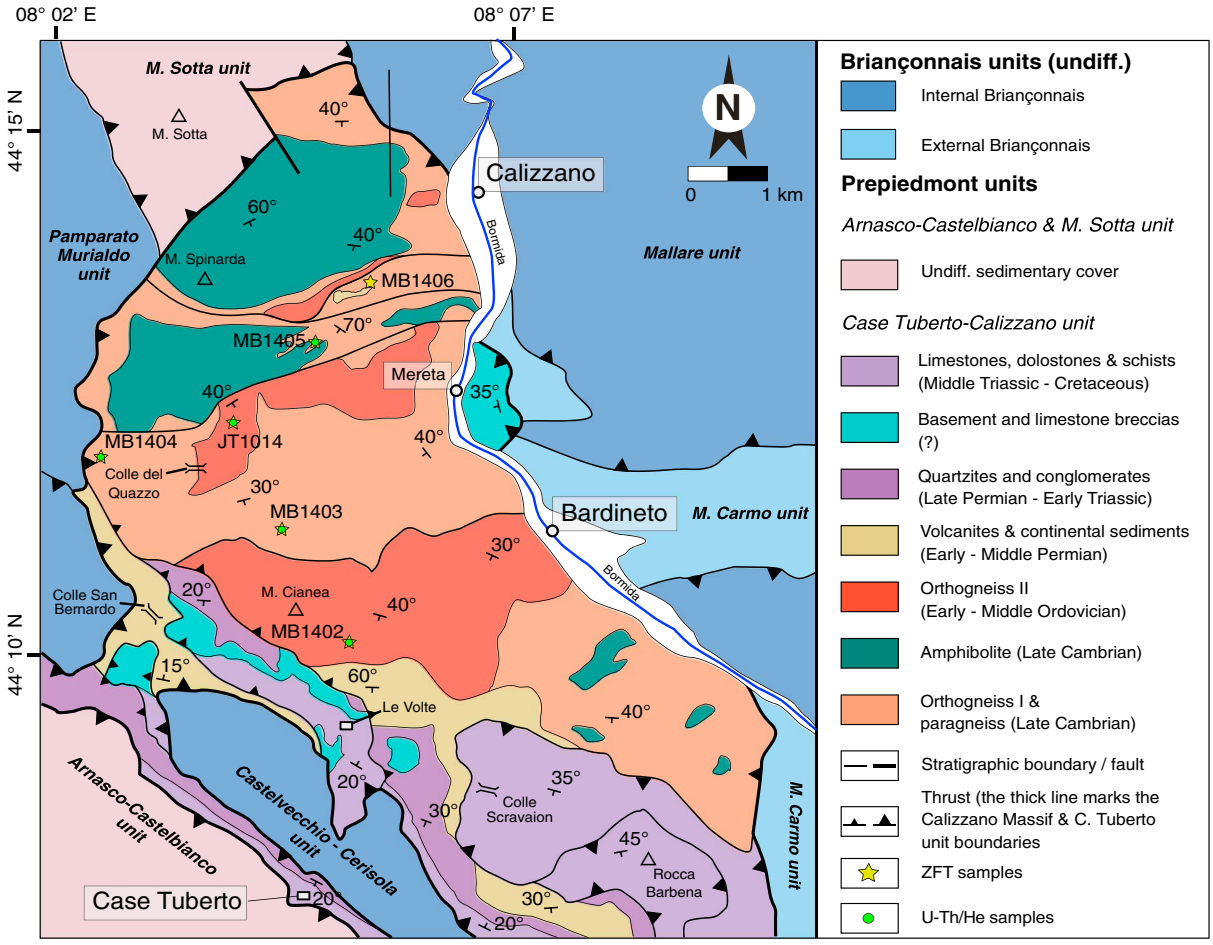

Figure 3. Geological map of the Case Tuberto-Calizzano unit and samples locations, modified from Seno et al. (2005a, 2005b).

(Dallagiovanna et al., 1984) to be a composite section due to the lack of a continuous field transect in which the different terrains are juxtaposed by indisputable stratigraphic boundaries. Its overall stratigraphic setting has been mostly determined by comparison with adjacent units of the Briançonnais and Prepiedmont domains. Thus, the total thickness of the Case Tuberto sedimentary cover (estimated as about 600 m) (Vanossi, 1991) should be considered a rough estimate, due to a number of factors, including (1) the above-described stratigraphic uncertainty; (2) the occurrence of Alpine low-T fabrics related to solution-precipitation processes, which likely modified the original thickness; and (3) the relatively low percentage of outcrop, preventing unambiguous assessment of the presence of second-order Alpine faults.

2.4. Case Tuberto-Calizzano Unit: Alpine Deformation and Metamorphism

The Alpine deformation developed through several events (Bonini et al., 2010; Maino et al., 2013; Seno et al., 2005a, 2005b), which are especially preserved in the sedimentary cover. The basement rocks record minor evidence of Alpine deformation, mostly represented by fracturing and fracture cleavage. The Meso-Cenozoic sedimentary succession shows two generation of folding and related cleavage (Dallagiovanna, 1988) (Figures 4a and 4b) associated with a widespread network of quartz veins. Basement rocks rarely preserve evidence of an Alpine overprint, which is characterized by different paragenesis in the different lithologies. Peak conditions are indicated by the following mineral associations: chlorite + albite + pumpellyite in the gneisses, chlorite + albite + epidote in the amphibolites, chlorite + phengite + pumpellyite + albite ± epidote (locally also lawsonite and Na-amphibole) in the Permian metavolcanites, chlorite + pumpellyite + albite ± mica + quartz in the Triassic quartzites, and sericite + chlorite in the Jurassic-Eocene pelites

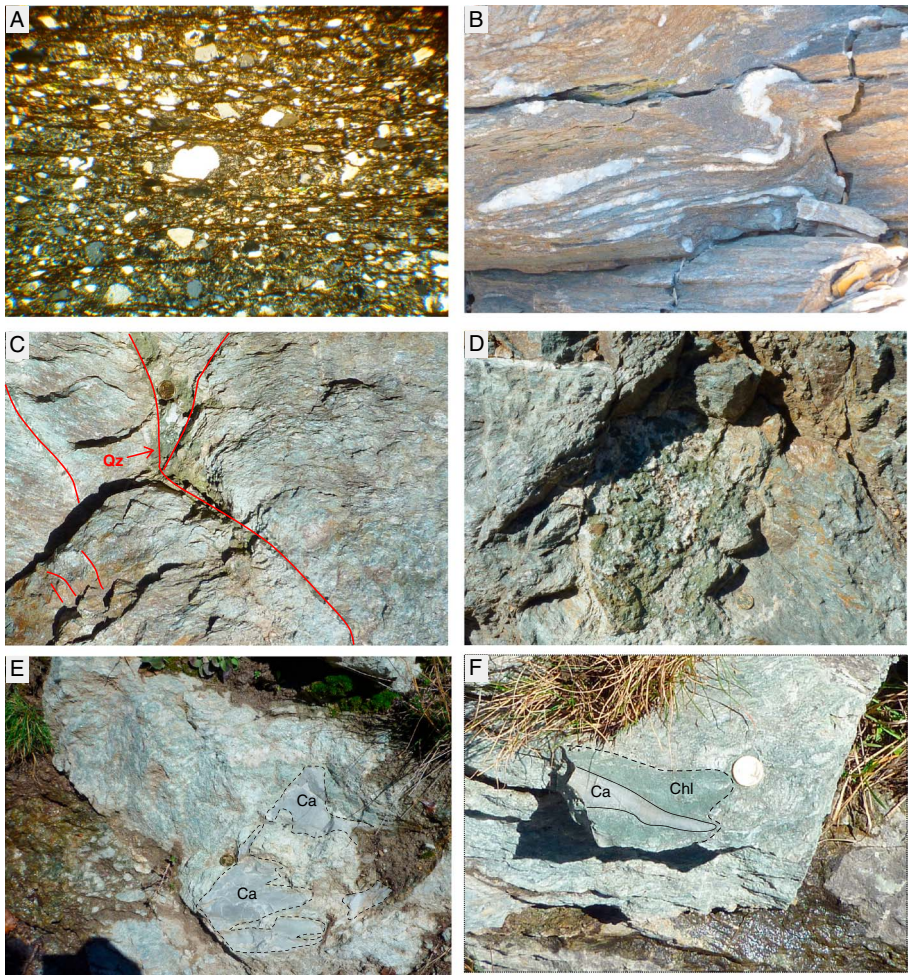

Figure 4. (a and b) Scravaion schist in the Type location (see Figure 2), showing pervasive Alpine deformation and related folded quartz veins network. (c and d) Quartz veins associated with widespread chlorite concentrations in the Orthogneiss I at the top of case Tuberto Calizzano basement unit. (e and f): Silicified breccia level lying on top of the orthogneiss near Calizzano village. Orthogneiss clasts are hardly distinguishable due to the pervasive silicification. Anastomosing carbonate clasts are locally associated to chlorite concentrations (Figure 4f).

(Cortesogno, 1984; Cortesogno et al., 1998, 2002; Desmons, Compagnoni et al., 1999; Desmons, Aprahamian et al., 1999; Messiga et al., 1981). These mineral assemblages suggest a wide range of P-T reequilibration conditions changing from prehnite-pumpellyite-, greenschist- to blueschist-facies conditions (pressure between 0.2 and 0.6 GPa and a temperature range between 250 and 400°C), in distinct lithologies and/or in different structural positions. In fact, most of the relatively high P-T condition assemblages are described in samples collected close to the main Alpine shear zone (e.g., Rio Nero and Case Volte). The highest temperatures were attained along major tectonic contacts, probably due to the effect of shear heating and/or fluid flow (Maino et al., 2015). However, the preservation of ^{40}Ar-^{39}Ar ages $>$274 Ma in white mica in analogous basement units (Savona and Nucetto massifs) (Barbieri et al., 2003) and one zircon fission track age of ~179 Ma (Vance, 1999) from the basement rocks suggests that the Alpine metamorphism probably did not exceed their relative closure temperatures (~350°C and ~240 ± 25°C, respectively) (Reiners & Brandon, 2006), thus questioning the effective temperature experienced by the Calizzano basement during the Alpine evolution. Because of the scarce Alpine relicts and the general lack of obvious relationships with the pre-Alpine associations and structures, it is not clear if these heterogeneous P-T conditions represent (i) a single Alpine stage differently recorded by different rocks, (ii) several Alpine stages; and (iii) several post-Variscan (i.e., not all Alpine) stages.

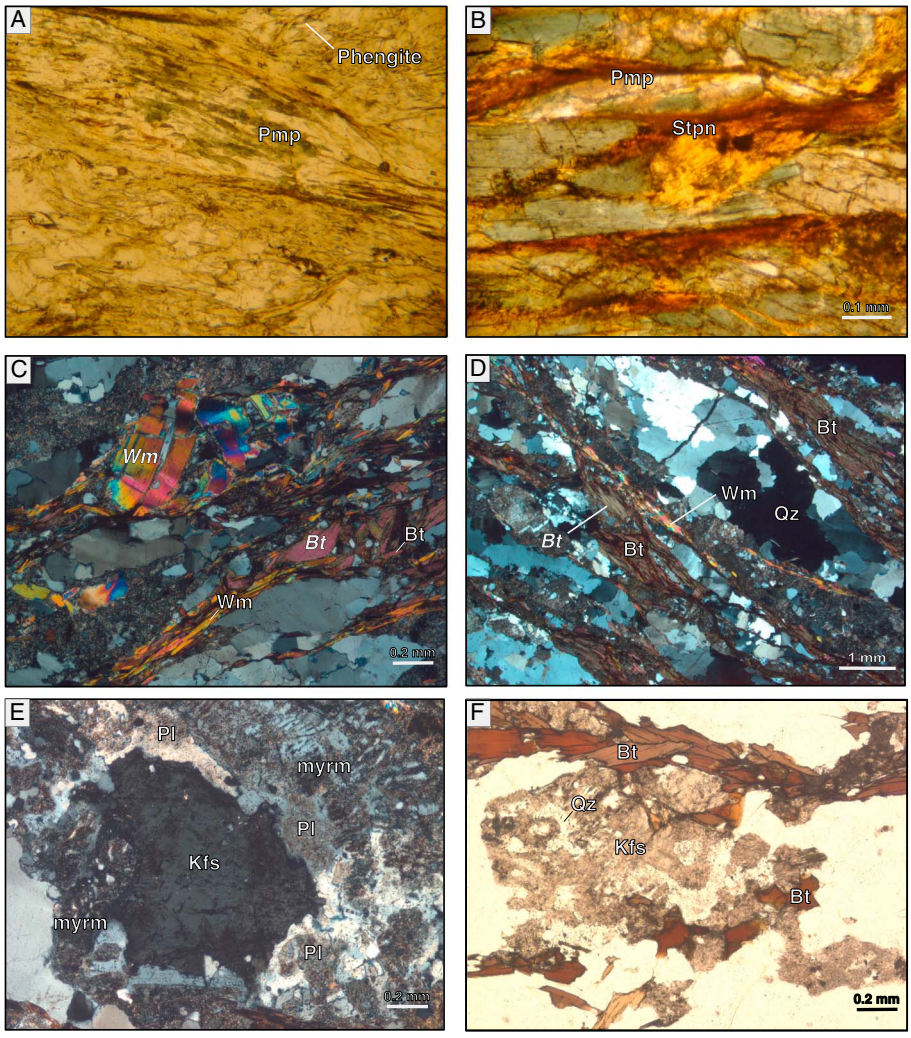

Figure 5. Microphotographs in transmitted light of the selected thin sections illustrating the main petrographic features of the different lithologies of the Case Tuberto-Calizzano basement. Plain polarized views of post-Variscan assemblages in amphibolites. (a) Pumpellyite and phengite, mimetic on the Variscan schistosity in leucocratic band. (b) Static blastesis of stilpnomelane and pumpellyite on hornblende + oligoclase Variscan assemblage. (c) Cross-polarized view of the two generations of white mica (Wm) and brown biotite (Bt) in the two-mica gneiss of the "gneiss-amphibolite complex." The older generation consists of large, deformed flakes (abbreviations in italic) locally defining an old foliation oriented approximately NNE-SSW in the picture. The younger generation consists of medium-grained lepidoblasts defining the main foliation oriented approximately NE-SW in the picture. (d) Cross-polarized view of an "Orthogneiss I" in which the main foliation is defined by brown biotite (Bt), white mica (Wm) and quartz ribbons (Qz). An older generation of biotite (in italic) is wrapped around by the main foliation. (e) Cross-polarized view of an "Orthogneiss I" showing a K-feldspar (Kfs) rimmed by plagioclase (Pl) and myrmekites (myrm). (f) Cross-polarized view of an "Orthogneiss II" in which a porphyroclastic K-feldspar (Kfs) including magmatic quartz (Qz) and brown biotite (Bt) is wrapped around by the main Variscan foliation defined by brown biotite.

3. Sample Description

Zircon fission track (ZFT) and (U-Th)/He (ZHe) analyses were carried out on seven samples collected from the Calizzano-Case Tuberto unit with the aim of constraining the thermal path experienced by the basement during the rifting and subsequent collisional stages. The samples correspond to Late Cambrian-Lower Ordovician orthogneiss I (samples MB1403-06) and Middle Ordovician orthogneiss II (MB1402 and JT1014), which experienced pre-Variscan and/or Variscan (Early Ordovician and Carboniferous, respectively) amphibolite facies metamorphism (Cortesogno, 1984; Gaggero et al., 2004).

3.1. Field Observations

In the sampling locations, the Variscan foliation in the orthogneisses is usually deformed and cut by distinct generations of millimeter- to centimeter-thick quartz veins (Figure 4c). These veins generally cut the deformed pre-Alpine foliation and comprise pure quartz or alternatively quartz with sharp chlorite bands at the contact with the host rock (Figure 4d). In addition, in selected localities this mineralization also affects the overlying sediments. Near Mereta and Calizzano villages (Figure 3), a breccia formed by orthogneisses and minor carbonate clasts directly covers the basement (Figure 4e). The clasts, from centimeter to meter in size, are characterized by sharp rounded edges. The breccia is so pervasively silicified that the boundary with the orthogneiss clasts is completely masked (Figure 4e). These features suggest a marked interaction with silicifying fluids circulating both inside the sampled basement rocks and in the overlying breccia.

3.2. Sample Petrography

We present analyses of three types of granites:

i. The first type (MB1405 sample) is a two-mica gneiss characterized by Variscan foliation defined by white mica and brown biotite, both medium-grained and undeformed. An older generation of coarser-grained, deformed white mica and brown biotite is wrapped around by the main foliation or defines a former foliation (Figure 5c). Medium-grained granoblastic quartz and poorly sericitized plagioclase are the other major rock-forming minerals. The textural and mineralogical features of this sample correspond to those of the paragneisses of the Gneiss-Amphibolite Complex (e.g., Cortesogno, 1984; Gaggero et al., 2004). Fine-grained static recrystallization of white mica (Figures 6a and 6b) and neoblastic growth of green biotite flakes (Figures 6d–6g), locally on former brown biotite (Figure 6c), occur along microshear zones crosscutting the main foliation (Figures 6a–6c and 6e). The green biotite has higher FeO_{tot} contents (20.37–22.14 wt %) and both lower TiO_2 contents (1.13–1.75 wt %) and TiO_2/MgO ratio (0.11–0.17) with respect to the brown biotite (FeO_{tot} = 18.52–20.56 wt %, TiO_2 = 2.21–3.06 wt %, and TiO_2/MgO = 0.23–0.35; Figure 5h and Table 2). Chlorite partly replaces both green and brown biotites (Figures 6a–6c, 6f, and 6g).
ii. The second type (MB1403, MB1404, and MB1406 samples) is represented by a two-mica augen-gneiss (Figure 5d) in which granoblastic, poorly sericitized K-feldspar is in equilibrium with a Variscan foliation defined by quartz ribbons and medium-grained white mica and biotite. An older generation of coarse-grained white mica and biotite also occurs. The K-feldspar is characterized by a rim of plagioclase and myrmekites (Figure 6e). These samples, which correspond to the Orthogneiss I of previous authors (e.g., Gaggero et al., 2004), do not show evidence for a late, greenschist-facies mineral assemblage.
iii. The third type (JT1014 and MB1402) is represented by a coarser-grained biotitic augen-gneiss (Figure 5f) in which only one generation of Variscan biotite, defining the main foliation, is present. The K-feldspar porphyroclasts, poorly sericitized, show magmatic inclusions of lobate quartz and subhedral biotite. In the studied samples, the local growth of white mica + chlorite partly replaces the former brown biotite. The lack of polyphase deformation and the relict magmatic microstructures indicate that these samples correspond to the Orthogneiss II of previous authors (e.g., Gaggero et al., 2004).

4. Methods

4.1. Biotite Chemical Composition

Compositions of brown and green biotite in sample MB1405 were obtained with a JEOL JSM IT300LV (high vacuum-low vacuum 10/650 Pa-0.3–30 kV) scanning electron microscopy equipped with an energy-dispersive spectroscopy Oxford INCA Energy 200 with detector INCA X-act SDD thin window at the Department of Earth Sciences, University of Torino. The operating conditions were as follows: 30 s counting time and 15 kV accelerating voltage. The quantitative data (spot size = 2 μm) were acquired and processed using the Microanalysis Suite Issue 12, INCA Suite version 4.01; natural mineral standards were used to calibrate the raw data; the ρφZ correction (Pouchou & Pichoir, 1988) was applied. Absolute error is 1σ for all calculated oxides.

4.2. Zircon Fission Track Dating

Zircon separates were mounted into Teflon pads, which were polished to expose internal surfaces. Two to three mounts per sample were prepared according to the availability of zircons in order to adopt the

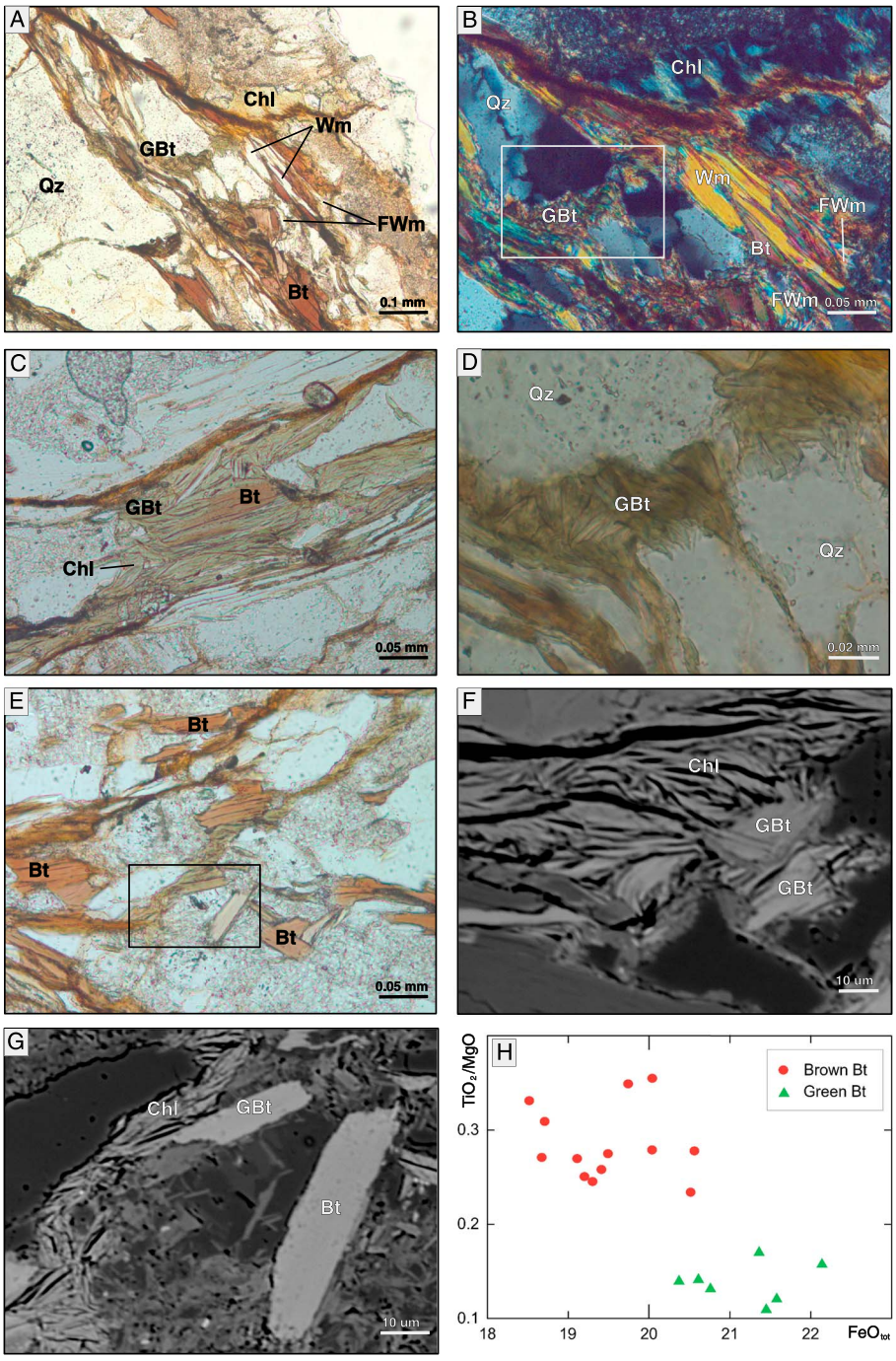

Figure 6. Microphotographs in transmitted light of the selected thin sections illustrating the post-Variscan growth of green biotite in the two-mica gneiss of the "gneiss amphibolite complex." (a) Plain and (b) cross-polarized view showing coarse-grained white mica (Wm) and brown biotite (Bt) defining the Variscan main foliation. (d) Both the partial recystallization of white mica into fine-grained flakes (FWm) and the local neoformation of aggregates of fine-grained green biotite (GBt) are recognizable. Chlorite (Chl), where present, is related to late fractures. (c) Plain-polarized view of a flake of brown biotite (Bt) partly replaced by green biotite (GBt) and, at the rim, by chlorite (Chl). (e) Plain-polarized view of the Variscan brown biotite (Bt) and of the younger green biotite flakes (GBt), partly replaced by chlorite (Chl), along (g) a microshear zone (detail in the backscattered image). (f) Backscattered image of the green biotite flakes (GBt) partly replaced by and aggregate of chlorite (Chl). (h) Compositions of both the brown and green biotite plotted in the TiO_2/Mg versus FeO_{tot} diagram (Engel & Engel, 1960).

Table 1
Zircon Fission Track Data

Sample/ mount	Location Lat	Location Long	Elevation (m)	Gr.	N_d track	ρd 1E + 05 track/cm^2	N_s track	ρs 1E + 07 track/cm^2	N_i track	ρi 1E + 06 track/cm^2	$P(\chi^2)$ %	Age dispersion %	Pooled Age ± σ1 Ma	Central Age ± σ1 Ma	Pop age -LCI + Ucl Ma	Fraction of gr. %	Age range
MB1402/a	44°10′36″	8°05′03″	1030	9	5277	3.9129	2303	1.5846	382	2.6283	1.75	20.53	168.6 ± 9.7	168.0 ± 14.9			103.8–300.8
MB1402/b				10	5238	3.8834											
MB1403/b	44°11′29″	8°04′55″	990	10	5158	3.8243	2051	1.7272	365	3.0737	74.85	1.67	153.4 ± 9.1	153.6 ± 11.6			94.5–271.8
MB1403/c				15	5118	3.7948											
MB1404/a	44°12′07	8°03′05″	970	38	5078	3.7653	4398	1.2824	726	2.1170	3.93	14.49	163.6 ± 7.0	163.8 ± 11.2			83.2–313.2
JT1014/b	44°12′40	8°04′21″	925	9	4779	3.5586	2474	1.2712	379	1.9474	22.34	8.77	165.9 ± 9.6	166.2 ± 13.0			107.6–292.3
JT1014/c				9	4760	3.5291											
MB1405/a	44°13′21	8°05′20″	800	24	4999	3.7062	3943	1.1781	759	2.2677	56.28	1.16	138.1 ± 5.8	138.1 ± 8.8			86.4–253.1
MB1405/b				12	4959	3.6767											
MB1406/a				30	4919	3.6472	6141	1.2204	1088	2.1622	19.66	9.14	147.3 ± 5.2	147.5 ± 9.0			85.3–339.0
MB1406/b				30	4879	3.6176									117.5–68.0 + 159.1	7	
ALL				196											150.6–15.2 + 17.0	93	
															128.7–32.9 - +41.1	21	
															156.2–32.9 + 41.5	71	
															214.9–43.5 + 54.3	8	

Note. ζ calibration factor: 145.39 ± 7.04.

multiple-etch technique of Naeser et al. (1987). The mounts were etched in a eutectic melt of NaOH and KOH at 228°C for either 7, 14, or 28 h. Mica laminae were attached to the samples as external detectors. The mounts were then irradiated at the Radiation Center of Oregon State University, using a nominal Neutron fluence of 1×10^{15} ncm^{-2}. Induced tracks were revealed by etching in 40% HF at 21°C for 45 min. Fission tracks were analyzed on all the countable grains from the 7 and 14 h etches, while the long etch resulted in overetched samples. The Fish Canyon tuff was used as a standard for the zeta calibration (Hurford & Green, 1983). The age distribution of the pooled ages of all samples were decomposed into dominant age peaks using the BinomFit program of Brandon (2002), version 1.2.63 (2007).

4.3. Zircon (U-Th)/He Dating

Zircon crystals were selected on the basis of size, morphology, and absence of inclusions. Crystals with two pyramidal terminations and undamaged surfaces were handpicked and their dimensions were measured. From each sample, one crystal was individually loaded into Pt-foil capsules. The average crystal widths ranged from 39.4 to 71 μm. Most of the selected grains have small radii because larger crystals are mostly affected by intense fracturing and/or presence of inclusions.

(U-Th)/He age determinations were performed at the Scottish Universities Environmental Research Centre. Complete helium extraction was achieved by heating the Pt foils using an 808 nm diode laser for 20 min at 1,100–1,300°C. ^{4}He concentrations were measured by peak height comparison to a calibrated standard using a Hiden HAL3F quadrupole mass spectrometer, following the protocols of Foeken et al. (2006). All samples were reheated two or three times to ensure complete degassing. U and Th determinations were made after extraction of the crystals from the Pt foil. The degassed zircons were spiked with a known amount of ^{235}U and ^{230}Th and dissolved in a Parr™ bomb acid digestion vessel. Ion exchange column chemistry was used to remove the Pt and other matrix elements. U and Th were measured on a VG PlasmaQuad-2 inductively coupled plasma–mass spectrometry. The calculated ages ("raw ages") have been corrected to account for He loss because of α-recoil (Ft; Farley et al., 1996) following the method of Ketcham et al. (2011). The uncertainty associated with the Ft correction factor calculation is propagated into the total uncertainty of the Ft-corrected (U-Th)/He ages.

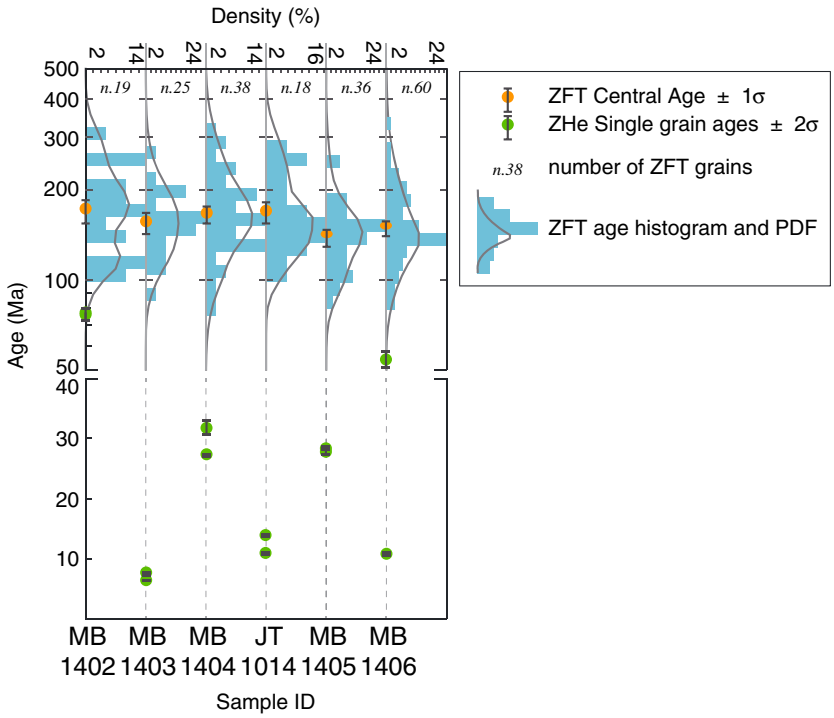

Figure 7. Zircon fission track and (U-Th)/He ages: samples are ordered according to their location from N to S. The distributions of the zircon fission track ages are also shown as histogram and as population density function (PDF) curves. The zircon fission track central ages overlap within the standard errors with the exception of samples MB1405, which is younger only if the 1σ error is considered. Within the 2σ error of the central ages, there is no significant difference. The (U-Th)/He ages show a large scatter that relates to incomplete age reset during the Alpine metamorphic overprint, to the large range of the eU content (Figure 9a), and of the grain dimensions.

An uncertainty of 11.9% (2σ) is assumed for individual age determination (Table 2), based on the age reproducibility of the Fish Canyon Tuff ZHe age standard (Dobson et al., 2008). The 2σ age reproducibility of each sample was also calculated. Apart from sample MB1406, all other samples have age reproducibility comparable to the zircon age standard. In order to constrain the time-temperature (t-T) history of selected samples, inverse modeling of the ZHe ages was performed using HeFTy (Ketcham, 2005). We have exploited the dependence of the He closure temperature (Tc) on grain size, cooling rate, and eU content (Reiners, 2005).

5. Results

5.1. Zircon Fission Track Data

Details of the sample ages and the age populations are reported in Table 1. All the count data and the radial plots are provided in the supporting information. The age distribution and the central age of each sample are plotted in Figure 7. Six samples provided enough zircons for fission track dating. Among these six samples, the amount of countable zircons is highly variable, from 18 to 60 grains per sample. The resulting central ages range from 138.1 to 168.6 Ma and average to 156.2 Ma with a standard deviation of 7%. The analytical error (1σ) of the central ages vary between 6% (MB1406) and 9% (MB1402), and five out six samples overlap within this error with the exception of sample MB1405, which is significantly younger than most samples (147.5 ± 9.0 Ma; Figure 7) only if the 1σ error or the 68% confidential intervals are considered. Two samples (MB1402 and MB1404) have a probability χ^2 value lower than 5% that indicates larger than expected Poissonian scatter in track count data. Thus, these two samples could consist of multiple age populations, whereas all the other samples consist of single-age populations. An extra Poissonian age scatter is often observed for zircon fission track age distribution even in samples that are expected to have a single-age population (e.g., Fellin et al., 2006). Such scatter can be partly attributed to the wide range in U concentrations typical of zircons, resulting in highly variable degree of radiation damage, which together with temperature

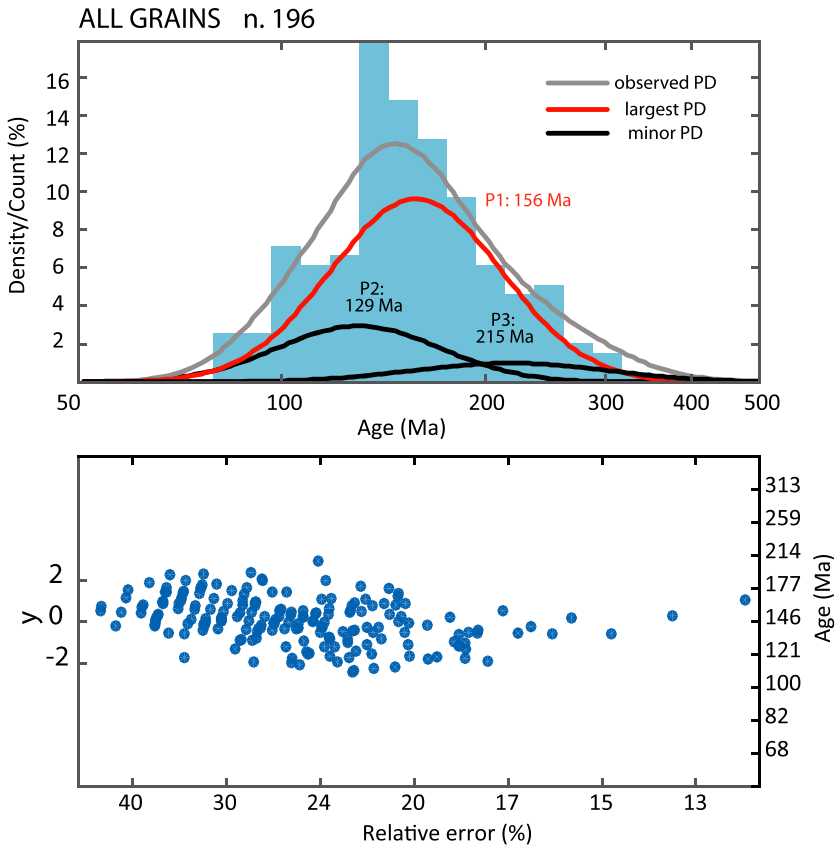

Figure 8. Radial plot and probability-density (PD) plot showing best fit peaks from Binomfit (Brandon, 2002, version 1.2.63 (2007)) for the pooled ages of all samples (all grains). *Y* is the 2σ standard error of the central age of the pooled grains. At least three age populations at 129, 156, and 215 Ma characterize the age distribution of the 196 zircons of the pooled samples.

controls the annealing of tracks. The number of countable grains in the two highly scattered samples is too low (19 and 38 grains) to derive statistically their age components. Their central and pooled ages have a difference of $<$1 Ma, which also indicate that multiple age populations cannot be resolved within these two samples. Thus, although different age populations cannot be resolved within individual samples, they could be resolved by pooling the grains together from all samples. The pooled grains amount to 196 and their distribution is formed by three age components (Figure 8). The largest population, formed by 71% of the grains, is centered at 156.2 Ma, which is exactly the same as the average of all the central ages of the samples. The other two populations are centered at 128.7 and 214.9 Ma and are formed by 21% and 7% of the grains, respectively. Thus, the average of the central ages of the samples and the main population of the pooled ages all consistently indicate a major age component at ~150–160 Ma. The young population at 128.7 Ma could relate to partial rejuvenation related to the Alpine overprint. The oldest population at 214.9 Ma could relate to zircons that are most resistant to annealing.

5.2. Zircon (U-Th)/He Data

Twelve ZHe age determinations performed on six samples (Table 2 and Figure 7) supplied five pairs of ages with reproducibility within the individual uncertainty (2σ). Reproducing ages range from 78 ± 9.3 to 6.9 ± 0.8 Ma. Sample MB1406 shows two very different ages (10.3 and 52.8 Ma) indicating poor reproducibility. Samples MB1404 and MB1405 are between 28.3 ± 3.3 and 29.4 ± 3.5 Ma, accordingly with the Oligocene Alpine ZHe ages reported from the other units of the Ligurian Alps (Maino, Dallagiovanna, Dobson et al., 2012; Maino et al., 2015). Samples MB1403 and JT1014 show younger ages (between 6.9 ± 0.8 and 12.6 ± 1.5 Ma) close to the AFT data reported in the study area (Foeken et al., 2003). Only the sample MB1402, collected close to the basement-cover boundary (Figure 2), has an old, pre-Alpine age of

AGU Tectonics

10.1002/2017TC004634

Table 2
Zircon (U-Th)/He Data

Sample/ aliquot	Location		Elevation (m)	Mean grain radius – Rs (μm)	U (ng)	Th (ng)	4He (ncc)	eU (ppm)	Analytical error %	Raw age (Ma)	Th/U	FT	Corrected age (Ma)
	Lat	Long											
MB1402/1	44°10′36″	8°05′03″	1030	61.5	2.74	0.36	2.1E − 08	7.50	3.11%	60.4	0.13	0.78	77.4
MB1402/2				71.0	1.06	0.23	8.6 E − 09	2.01	5.06%	62.8	0.21	0.80	78.5
Mean ZHe age													78 ± 9.3
MB1403/1	44°11′29″	8°04′55″	990	47.1	4.05	1.05	2.4 E − 09	28.90	1.19%	4.6	0.26	0.72	6.6
MB1403/2				39.5	14.61	0.45	9.4 E − 09	151.69	2.50%	5.3	0.03	0.69	7.3
Mean ZHe age													6.9 ± 0.8
MB1404/1	44°12′07″	8°03′05″	970	38.2	9.15	2.95	2.2 E − 08	114.08	0.60%	18.5	0.32	0.68	26.8
MB1404/2				48.3	3.71	0.14	1.1 E − 08	21.67	7.64%	23.4	0.04	0.74	31.2
Mean ZHe age													29.0 ± 3.4
JT1014/1	44°12′40″	8°04′21″	925	44.1	3.58	0.67	4.6 E − 09	27.82	1.75%	10.0	0.19	0.72	13.5
JT1014/2				47.5	17.21	2.86	1.8 E − 08	111.66	0.59%	8.1	0.17	0.74	11.6
Mean ZHe age													12.6 ± 1.5
MB1405/1	44°13′21″	8°05′20″	800	33.4	3.73	0.65	8.5 E − 09	69.23	1.79%	18.0	0.17	0.65	26.9
MB1405/2				34.8	13.14	1.95	3.1 E − 08	218.71	0.72%	18.7	0.15	0.66	27.5
Mean ZHe age													27.2 ± 3.2
MB1406/1	44°13′49″	8°05′56″	880	42.9	7.36	8.38	9.2 E − 09	31.79	4.09%	8.1	1.14	0.70	11.6
MB1406/2				48.8	4.59	0.69	2.3 E − 08	27.03	1.67%	39.6	0.15	0.75	52.8
													ND
FCT/1				40.4	2.11	1.29	5.2 E − 09		1.61%	17.6	0.61	0.68	25.9
FCT/1				65.9	1.99	1.41	7.2 E − 09		1.60%	25.6	0.71	0.80	32.0
Mean ZHe age													29.0 ± 3.4

Note. Single-crystal aliquots were used for all samples. U and Th data are corrected for a procedural blank of 0.1067 ng U and 0.0997 ng Th. Blank uncertainty is ±10% and is included in the analytical uncertainty. The main grain radius (Rs) is derived from the mass weighted average radius (MWAR). eU is the effective uranium content computed as [U] + 0.235[Th]. ZHe ages are corrected for the recoil correction, FT, calculated using the calculations of Ketcham et al. (2011) assuming homogeneity. FCT is the Fish Canyon Tuff standard. Age uncertainties from ZHe age measurement are 11.9% (calculated from the 2σ age reproducibility of the FCT age standard). ND indicates not determined.

78 ± 9.3 Ma. Noticeably, this sample has the largest mean crystal radii (61.5–71 μm), suggesting a positive correlation between grain size and age. The considerably different ages from samples without relevant differences of elevation or structural position can be ascribed to many factors influencing the sensitivity of the (U-Th)/He system, including radiation damage (Flowers et al., 2007; Guenthner et al., 2013), the accuracy of the Ft correction (Reiners et al., 2011), U and Th zonation (Dobson et al., 2008), and the residence time of zircons within the partial retention zone (150–220°C) (Guenthner et al., 2013; Reiners et al., 2004). These factors can influence the results particularly for zircons that experienced a complex geological history as in our case. In particular, a high radiation damage accumulation is suggested by the negative date-effective uranium (eU) correlation (Guenthner et al., 2013) derived from the analyzed zircons (Figure 9a). Furthermore, the ZHe ages show a strong positive correlation with the grain sizes (Figure 9b), where the largest crystals were not reset, thus suggesting that the zircons experienced temperatures close to the lower boundary of the partial retention zone.

6. Discussion

ZFT single-grain ages from the Case Tuberto-Calizzano unit span a large age range from 340 to 83 Ma. These ages fill the gap between the Rb/Sr and $^{40}Ar/^{39}Ar$ ages (327–274 Ma in the Briançonnais-Prepiedmont units; Barbieri et al., 2003; Del Moro et al., 1982) and the ZHe ages (78–7 Ma; Maino, Dallagiovanna, Dobson, et al., 2012; this study).

The large ZFT age range can be partly related simply to the Poissonian age scatter typical of fission track data, but it could also reflect a long residence time of the studied rocks in the ZFT partial annealing zone that would result in a wide annealing degree. The consistency among the central ages, and between those ages and the age of the largest population (71%) of the pooled grains, indicates that cooling below the ZFT closure temperature (~240°C; Brandon et al., 1998) likely occurred at around 150–160 Ma. The dependency between closure temperature and cooling rate and the general shortage of constraints available on the thermal history of the studied rocks make it difficult to derive the temperature at which closure of our ZFT ages occurred. In fact, for cooling rates in the order of 10°C/km, the closure temperature is ~240°C (Reiners & Brandon, 2006), but for slow cooling of 0.6°C/Myr, it is as low as 205°C (Bernet, 2009). Nevertheless, the timing of cooling as constrained by our ZFT data indicates that the Jurassic rifting is a possible reason for the heating/cooling cycle. The lower ZFT annealing zone overlaps with the upper ZHe retention zone at temperatures higher than ~180°C such that the temperatures required to attain incomplete reset of the ZHe ages may cause partial rejuvenation of the most sensitive zircons and therefore may explain some of the youngest ZFT ages observed in our samples.

Tertiary ages for the Alpine metamorphism are heterogeneously recorded by the ZHe ages, suggesting partial to total resetting. While the ages between 29 and 7 Ma fit with the Alpine regional cooling ages (Foeken et al., 2003; Maino, Dallagiovanna, Dobson, et al., 2012), the ages between 78 and 53 Ma are considerably older. This wide variation is probably due to high radiation damage accumulation, as indicated by the negative date-effective uranium (eU) correlation and the positive grain size/age correlation (Figures 9a and 9b and Table 2). The ZHe age thermal model corroborates that the Alpine tectono-metamorphic phases were attained in a short interval at low-T condition (Figure 9c), not sufficient to completely reset the ZHe ages (i.e., temperatures were around 180°C for a few Myr).

However, mineral parageneses indicate Alpine metamorphism at T ~250–400°C. Such temperatures are considerably higher than those required to completely reset both ZHe and ZFT ages. Therefore, an apparent discrepancy exists between the constraints derived from the metamorphic assemblages and those based on the degree of resetting of the thermochronometric ages. In order to reconcile the different lines of evidence, we should consider—as first point—the distribution of the Alpine metamorphic record, which is locally recorded mostly along shear zones; it does not pervade the rocks and it is characterized by highly variable paragenesis in different lithologies and locations (Messiga et al., 1981). Most of the Calizzano and Case Tuberto rocks show evidence of low-T (prehnite-pumpellyite facies) Alpine metamorphism and deformation (fracturing and fracture cleavage). Indeed, the higher P-T parageneses (greenschist-to-blueschist facies) have been found mostly along Alpine shear zones, suggesting the possible influence of local heating (and pressure increase) associated with focused deformation (e.g., Maino et al., 2015). This suggests

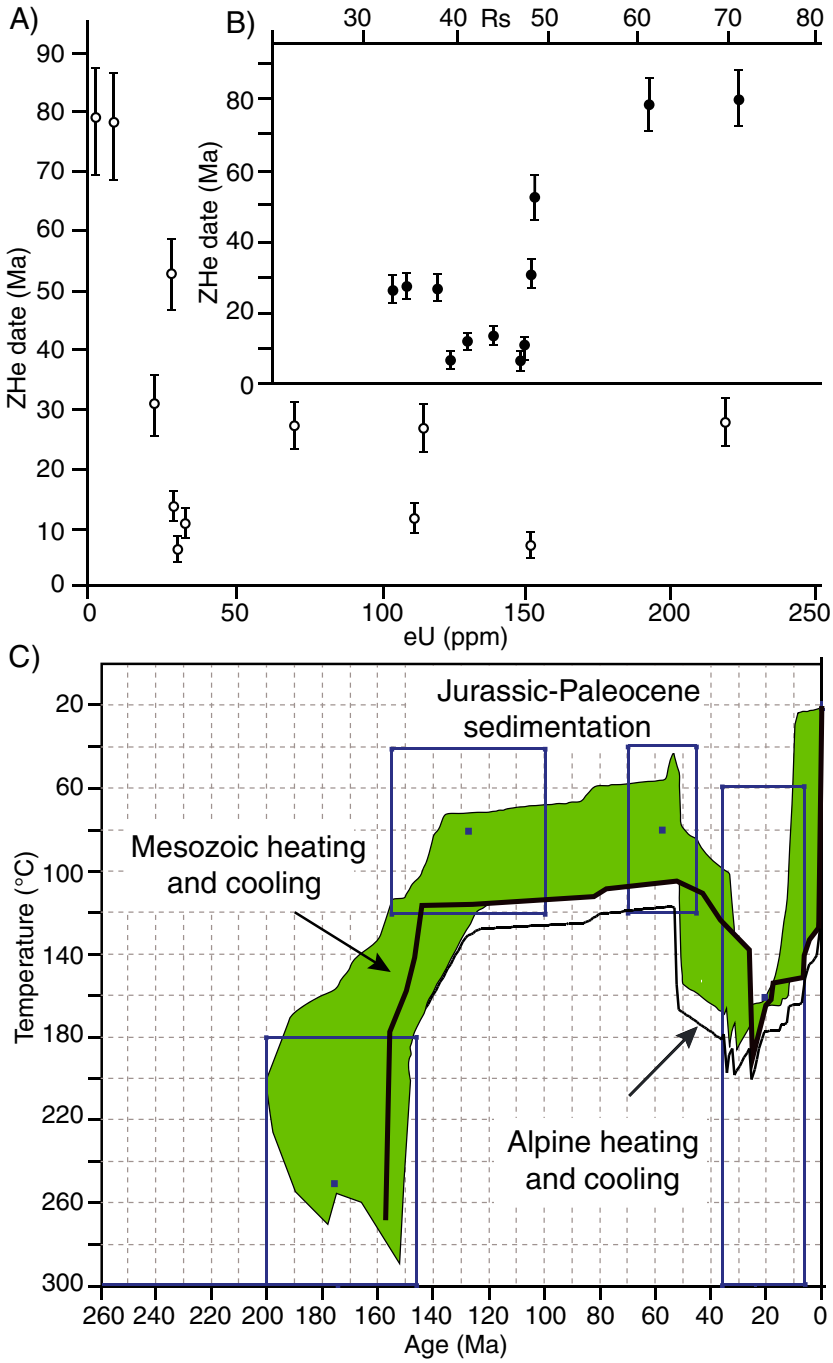

Figure 9. (a) Negative date-eU correlation of the analyzed samples. Individual points in each data set represent single ages (2 sigma error). (b) Positive date-grain size (Rs = 3*volume/surface) correlation. (c) ZHe thermochronometric inverse modeling results of samples MB1402 and MB1404. Acceptable time-temperature paths (green area) and best fit solution (black line) determined by Hefty program (Ketcham, 2005) using the initial constrains of the ZFT ages (this study) and Jurassic-Eocene depositional age of the basement cover (Vanossi et al., 1986).

that far from sites of high strain where higher P-T conditions were attained, the Alpine metamorphism may have developed as a low-T thermal pulse.

A second possible explanation for the discrepancy between metamorphic and thermochronometric record is that part of the paragenesis previously ascribed to the Alpine stage was developed during a pre-Alpine (but

post-Variscan) thermal event. In the study area, the Variscan cycle ends with a greenschist-facies folding event developing actinolite + chlorite along axial planes (Gaggero et al., 2004). In lithologies with suitable bulk composition, the growth of green biotite along microshear zones crosscutting Variscan microstructures, and its partial replacement by Alpine chlorite along fractures (Figure 6), records a tectono-metamorphic event that occurred between the Variscan and Alpine orogeneses. It is known that a systematic change in biotite color from greenish-brown to reddish-brown/black occurs with increasing metamorphism and is due to variations in chemical composition (Engel & Engel, 1960). In particular, the greenish color is produced by high Fe_{tot} coupled with low TiO_2/MgO ratio (Figure 5h) and it is indicative of low metamorphic grade (Engel & Engel, 1960; Henry et al., 2005). In fact, in suitable lithologies, the formation of prograde green biotite at low metamorphic grade can occur as a result of reactions involving K-feldspar and chlorite (Verschure et al., 1980) and its presence can be taken as indicative of temperatures around 350–450°C (Blanckenburg et al., 1989; Bozkurt et al., 2011; Del Moro et al., 1982; Jäger, 1967; Satır & Friedrichsen, 1986; Verschure et al., 1980). Thus, the green biotite indicates that the studied area experienced a post-Variscan, pre-Alpine heating event at HT greenschist-facies conditions during the extensional regime. A similar event is also recorded in phyllonites containing green biotite, formed along a Jurassic detachment in the distal margin represented by the Canavese Zone (Western Alps; Ferrando et al., 2004).

We infer that in the study area, an anomalously high geothermal gradient coupled with a pervasive circulation of hot fluids were responsible for the quartz mineralization (Figure 4) and for the growth of green biotite in suitable lithologies (Figure 6).

Such conditions could be met in an extended rift system where heating/cooling cycles are typically coupled with focused thinning, high geothermal gradients (~60–90°C/km; Hart et al., 2017; Liao et al., 2014; Vacherat et al., 2014), and circulation of hot fluids. Moreover, these thermal conditions could explain the growth of the less diagnostic assemblage chlorite ± white mica in other lithologies of the study area. Our ZFT ages support this interpretation as they indicate that temperatures above ~200°C must have extensively affected the study area before 150–160 Ma. Thus, we suggest that at least part of the Alpine greenschist facies mineral assemblage reported by the previous studies in the Calizzano basement rocks (Cortesogno et al., 1998; Messiga et al., 1981) needs to be explained by invoking heating mechanisms other than the Alpine metamorphism and may be linked, instead, to Tethys rifting. An accurate estimate of the Jurassic burial depth of the sampled basement is difficult given the poor preservation of the synrift sedimentary record. Regardless, the sampled basement was probably located at shallow depth during rifting as we estimate that our most superficial basement samples were probably at less than 2–3 km below synrift sediments. Assuming a surface temperature between 10 and 20°C and a geothermal gradient of 80°C/km, typical of hyperextended margins (Hart et al., 2017; Vacherat et al., 2014), this depth corresponds to temperatures between ~170 and 260°C, which are in the range of the ZFT partial annealing zone (~200–260°C; Reiners & Brandon, 2006). Furthermore, circulating fluids, possibly within crustal fault systems, may have affected heat transfer at such shallow crustal levels. A similar mechanism was proposed by Beltrando et al. (2015) to explain the cooling ages of the distal margin exposed in the Southalpine domain of the Alps.

To decipher the significance of the above-described scenario in the Case Tuberto-Calizzano unit at the scale of the European rifted margin, the paleo-structural location within an Alpine rift of this nappe must be considered (Figure 10). In the section proposed by Decarlis et al. (2015) across the European margin exposed in Liguria, the Case Tuberto-Calizzano unit is located at the boundary between the Briançonnais and Prepiedmont domains (see Decarlis et al., 2013; Vanossi, 1991). This domain was characterized by one of the major fault systems that accommodated crustal thinning within the future distal margin (i.e., φ fault in Figure 10). This fault system controlled the development of the distal margin juxtaposing the elevated and uplifted Briançonnais block (Decarlis & Lualdi, 2008) against the delaminated and strongly subsiding Prepiedmont domain (Decarlis & Lualdi, 2011) during the late Early Jurassic. During the Middle Jurassic, the emerged sector of the distal margin drowned, as testified by the renewal of deposition atop (Decarlis et al., 2013; Decarlis & Lualdi, 2008), and deformation migrated toward the future ocean along a detachment system initiating active exhumation (ε fault in Figure 10).

In a rift model such as that shown in Figure 10, the Case Tuberto-Calizzano unit might have been passively affected by a heating event induced by the combined action of crustal/lithospheric thinning and the activation of hydrothermal systems along brittle faults (φ-like). Fault systems might have played a first-order role in

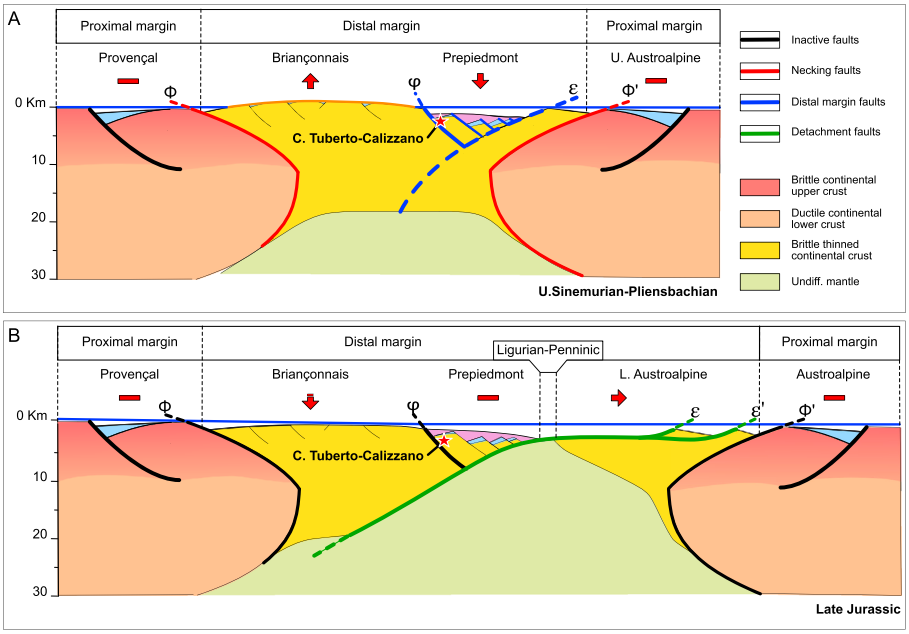

Figure 10. Supposed location of the sampling sites within Case Tuberto-Calizzano unit during the Alpine Tethys rifting, and suggested tectonic evolution within the distal margin, modified from Decarlis et al. (2015). (a) Upper Sinemurian-Pliensbachian stage: the distal margin was progressively thinned and became tectonically active. The Briançonnais domain was uplifted under subaerial conditions, while Prepiedmont domain, separated by the φ fault system, remained in submerged and progressively drowning marine environment. (b) Late Jurassic stage: after subcontinental mantle exhumation at the seafloor through the ε detachment fault system (Ligurian-Penninic domains), Briançonnais subsided, and tectonics ceases along the distal margin.

transporting heat toward the surface through remobilization of deep-seated fluid circulation during the final stages of rifting (i.e., during the thinning phase: Pliensbachian-Toarcian). Subsequent tectonic quiescence of the fault system during the Middle Jurassic, due to lithospheric onset of exhumation, led to the progressive cooling of the distal margin that is recorded by the ZFT data. A similar timing for active hydrothermal fluid systems associated with Jurassic rifting in the distal Alpine Tethys margin has been recently proposed by Incerpi et al. (2017).

Thus, both the present study and the literature data suggest that relatively high temperatures (between ~200 and 400°C) might have been acquired during crustal/lithospheric thinning driven by fluid activity in the upper crust at different locations along the Alpine Tethys distal margins (e.g., Beltrando et al., 2015; Incerpi et al., 2017). Our study demonstrates that such conditions were able to generate metamorphic paragenesis (greenschist facies) at very shallow crustal levels of $<$2–3 km. The temperature peak was reached during the formation of the future distal margin and cooling initiated at the onset of exhumation and migration of active tectonics further oceanward.

7. Conclusions

Thermochronometric analysis of basement rocks belonging to the Case Tuberto-Calizzano unit led to the recognition of two distinct heating-cooling cycles that have been respectively attributed to the Alpine Tethys rifting stage (ZFT ages of ~150–160 Ma) and to the Alpine orogenic deformation (ZHe ages of ~29.4 to 7 Ma). These data coupled with the local growth of green biotite (stable at about 350–450°C) in lithologies with suitable bulk composition and evidence for abundant mineralization suggest that the temperatures reached during the rifting stage exceeded those of the Alpine metamorphism in the study area. The incomplete reset of the ZHe ages and the nonreset of the ZFT ages during the Alpine metamorphism indicate that the well-documented Alpine deformation had to occur under conditions from prehnite-pumpellyte to low-temperature blueschists facies at temperatures lower than ~200°C. Thus, the Alpine metamorphic overprint must have occurred during a short-lived low-temperature pulse. The lack of pervasive Alpine resetting of the

ages allowed the preservation of an older heating-cooling event that occurred during Alpine Tethys rifting. Considering the peculiar position of the study area in the former Jurassic rifted margin, heating may have been caused by the combined effect of severe crustal/lithospheric thinning in the distal domain associated with high geothermal gradients and hydrothermal circulation along brittle faults. This latter might have focused hot deep-seated fluids toward shallow crustal levels, which are represented by the studied Case Tuberto-Calizzano unit (samples located at less than 2–3 km depth during rifting), causing basement heating during the thinning phase (Pliensbachian-Toarcian) with a similar mechanism to that suggested by Beltrando et al. (2015). The following stages of rifting, i.e., the beginning of exhumation in the more distal parts of the distal margin, resulted in a tectonic quiescence (probably since the Bajocian-Bathonian) and progressive cooling of the basement that was recorded by the Middle Jurassic ZFT ages and completed during the Late Jurassic. The rift-related heating, often difficult to recognize in mountain belts due to the orogenic overprint, can be recognized in the Case Tuberto-Calizzano unit. Therefore, this latter unit can be considered as an excellent "fossil analogue" within which future research may qualitatively and qualitatively estimate the thermal evolution and heat transfer mechanisms occurring at distal magma-poor rifted margins during final rifting and plate separation.

Acknowledgments
We gratefully thank Philip Ball, Virginia Toy, and two anonymous reviewers for helpful reviews that significantly improve the manuscript. The research was supported by Torino University grant (Torino_call2014_L1_202; Resp. S.F.) and by MM4 consortium (Margin Modeling Phase 4: Liverpool and Strasbourg University), taking benefits from useful discussions with colleagues from the academic and industrial partners. The data supporting this paper are available within tables, figures, and supporting information section.

References

Airoldi, M. (1937). Rilevamenti geologici nelle Alpi Liguri. II. Il Massiccio di Calizzano. *Bollettino della Societa Geologica Italiana*, *56*, 467–498.

Barbieri, C., Carrapa, B., Di Giulio, A., Wijbrans, J., & Murrell, G. (2003). Provenance of Oligocene synorogenic sediments of the Ligurian Alps (NW Italy): Inferences on belt age and cooling history. *International Journal of Earth Sciences*, *92*(5), 758–778. https://doi.org/10.1007/s00531-003-0351-x

Beltrando, M., Stockli, D. F., Decarlis, A., & Manatschal, G. (2015). A crustal-scale view at rift localization along the fossil Adriatic margin of the Alpine Tethys preserved in NW Italy. *Tectonics*, *34*, 1927–1951. https://doi.org/10.1002/2015TC003973

Bernet, M. (2009). A field-based estimate of the zircon fission-track closure temperature. *Chemical Geology*, *259*, 181–189.

Blanckenburg, V. F., Villa, I. M., Baur, H., Morteani, G., & Steiger, R. H. (1989). Time calibration of a PT-path from the Western Tauern Window, Eastern Alps: The problem of closure temperatures. *Contributions to Mineralogy and Petrology*, *101*(1), 1–11. https://doi.org/10.1007/BF00387196

Bonini, L., Dallagiovanna, G., & Seno, S. (2010). The role of pre-existing faults in the structural evolution of thrust systems: Insights from the Ligurian Alps (Italy). *Tectonophysics*, *480*(1-4), 73–87. https://doi.org/10.1016/j.tecto.2009.09.021

Bozkurt, E., Satır, M., & Buğdaycıoğlu, Ç. (2011). Surprisingly young Rb/Sr ages from the Simav extensional detachment fault zone, northern Menderes massif, Turkey. *Journal of Geodynamics*, *52*(5), 406–431. https://doi.org/10.1016/j.jog.2011.06.002

Brandon, M. T. (2002). Decomposition of mixed grain age distributions using BINOMFIT. *On Track*, *24*, 1–18.

Brandon, M. T., Roden-Tice, M. K., & Garver, J. I. (1998). Late Cenozoic exhumation of the Cascadia accretionary wedge in the Olympic Mountains, northwest Washington State. *Geological Society of America Bulletin*, *110*(8), 985–1009.

Capponi, G., & Crispini, L. (2002). Structural and metamorphic signature of alpine tectonics in the Voltri massif (Ligurian Alps, North-Western Italy). *Eclogae Geologicae Helvetiae*, *95*, 31–42.

Claudel, M. E., & Dumont, T. (1999). A record of multistage continental break-up on the Briançonnais marginal plateau (Western Alps): Early and Middle Jurassic rifting. *Eclogae Geologicae Helvetiae*, *92*, 45–61.

Cortesogno, L. (1984). Metamorfismo e magmatismo prealpini nel basamento e nel tegumento delle Alpi Liguri. *Memorie della Societa Geologica Italiana*, *28*, 79–94.

Cortesogno, L., Dallagiovanna, G., Gaggero, L., & Vanossi, M. (1993). Elements of the Palaeozoic history of the Ligurian Alps. In J. F. von Raumer & F. Neubauer (Eds.), *Pre-Mesozoic Geology in the Alps* (pp. 257–277). Berlin, Heidelberg: Springer. https://doi.org/10.1007/978-3-642-84640-3_15

Cortesogno, L., Dallagiovanna, G., Gaggero, L., Seno, S., & Vanossi, M. (1998). Tettonica vulcanismo tardo-Paleozoici nel dominio prepiemontese delle Alpi Liguri: la testimonianza della successione del Colle Scravaion. *Atti Ticinesi Scienze della Terra*, *7*, 17–26.

Cortesogno, L., Gaggero, L., Lucchetti, G., & Cabella, R. (2002). Compositions and miscibility gap in Na-Ca clinopyroxenes through high-pressure metamorphism. *Personality Mineral*, *71*(1), 1–25.

Crozi, M. (1998). Basamento e coperture prepiemontesi tra il colle di San Bernardo ed il colle Scravaion (alpi Liguri): precisazioni stratigrafiche e strutturali, M.S. thesis, Department of Earth Sciences, University Of Pavia, Italy

Dallagiovanna, G. (1988). Testimonianze e significato di una trasgressione permo-triassica sul basamento cristallino del Brianzonese Ligure Interno. *Bollettino della Societa Geologica Italiana*, *107*, 445–451.

Dallagiovanna, G., & Seno, S. (1984). Rilevamento geologico ed analisi strutturale del settore meridionale dell'unita` di Arnasco-Castelbianco (Alpi Marittime). *Memorie della Societa Geologica Italiana*, *28*, 441–445.

Dallagiovanna, G., Lualdi, A., Seno, S., & Vanossi, M. (1984). Nuovi dati e precisazioni sull'Unità di C. Tuberto (Prepiemontese delle Alpi Liguri). *Memorie della Societa Geologica Italiana*, *28*, 419–430.

Dallagiovanna, G., Gaggero, L., Maino, M., Seno, S., & Tiepolo, M. (2009). U–Pb zircon ages for post-Variscan volcanism in the Ligurian Alps (Northern Italy). *Journal of the Geological Society*, *166*(1), 101–114. https://doi.org/10.1144/0016-76492008-027

De Graciansky, P. C., Roberts, D. G., & Tricart, P. (2011). *The Western Alps, from rift to passive margin to orogenic belt: An integrated geoscience overview*, *Developments in Earth Surface Processes* (Vol. 14, p. 397). Amsterdam: Elsevier. https://doi.org/10.1016/c2009-0-64485-8

Decarlis, A., & Lualdi, A. (2008). Late Triassic-Early Jurassic paleokarst from the Ligurian Alps and its geological significance (Siderolitico Auct., Ligurian Briançonnais domain). *Swiss Journal of Geosciences*, *101*(3), 579–593. https://doi.org/10.1007/s00015-008-1302-0

Decarlis, A., & Lualdi, A. (2011). Synrift sedimentation on the northern Tethys margin: An example from the Ligurian Alps (Upper Triassic to Lower Cretaceous, Prepiedmont domain, Italy). *International Journal of Earth Sciences*, *100*(7), 1589–1604. https://doi.org/10.1007/s00531-010-0587-1

Decarlis, A., Dallagiovanna, G., Lualdi, A., Maino, M., & Seno, S. (2013). Stratigraphic evolution in the Ligurian Alps between Variscan heritages and the Alpine Tethys opening: A review. *Earth-Science Reviews*, *125*, 43–68. https://doi.org/10.1016/j.earscirev.2013.07.001

Decarlis, A., Maino, M., Dallagiovanna, G., Lualdi, A., Masini, E., Toscani, G., & Seno, S. (2014). Salt tectonics in the SW Alps (Italy–France): From rifting to the inversion of the European continental margin in a context of oblique convergence. *Tectonophysics*, *636*, 293–314. https://doi.org/10.1016/j.tecto.2014.09.003

Decarlis, A., Manatschal, G., Haupert, I., & Masini, E. (2015). The tectono-stratigraphic evolution of distal, hyper-extended magma-poor conjugate rifted margins: Examples from the Alpine Tethys and Newfoundland Iberia. *Marine and Petroleum Geology*, *68*, 54–72. https://doi.org/10.1016/j.marpetgeo.2015.08.005

Decarlis, A., Beltrando, M., Manatschal, G., Ferrando, S., & Carosi, R. (2017). Architecture of the distal Piedmont-Ligurian rifted margin in NW-Italy: Hints for a flip of the rift system polarity. *Tectonics*, *36*, 2388–2406. https://doi.org/10.1002/2017TC004561

Del Moro, A., Pardini, G., Messiga, B., & Poggio, M. (1982). Dati petrologici e radiometrici preliminari sui massicci cristalllini della Liguria Occidentale. *Rendiconti della Società Italiana di Mineralogia e Petrografia*, *38*(1), 73–87.

Del Moro, A., Puxeddu, M., Radicati di Brozolo, F., & Villa, I. M. (1982). Rb-Sr and K-Ar ages on minerals at temperatures of 300–400°C from deep wells in the Larderello geothermal field (Italy). *Contributions to Mineralogy and Petrology*, *81*(4), 340–349. https://doi.org/10.1007/BF00371688

Desmons, J., Compagnoni, R., Cortesogno, L., Frey, M., & Gaggero, L. (1999). Pre-Alpine metamorphism of the internal zones of the Western Alps. *Schweizerische Mineralogische und Petrographische Mitteilungen*, *79*, 23–39.

Desmons, J., Aprahamian, J., Compagnoni, R., Cortesogno, L., Frey, M., Gaggero, L., … Seno, S. (1999). Alpine metamorphism of the Western Alps: I. Middle to high T/P metamorphism. *Schweizerische Mineralogische und Petrographische Mitteilungen*, *79*, 89–110.

Dobson, K. J., Stuart, F. M., Dempster, T. J., & EIMF (2008). U and Th zonation in Fish Canyon Tuff zircons: Implications for a zircon (U-Th)/He standard. *Geochimica et Cosmochimica Acta*, *72*(19), 4745–4755. https://doi.org/10.1016/j.gca.2008.07.015

Engel, A. E. J., & Engel, C. (1960). Progressive metamorphism and granitization of the major paragneiss, northwest Adirondack Mountains, New York: Mineralogy. *Geological Society of America Bulletin*, *71*(1), 1–58. https://doi.org/10.1130/0016-7606(1960)71%5B1:PMAGOT%5D2.0.CO;2

Farley, K. A., Wolf, R. A., & Silver, L. T. (1996). The effects of long alpha-stopping distances on (U-Th)/He ages. *Geochimica et Cosmochimica Acta*, *60*(21), 4223–4229. https://doi.org/10.1016/S0016-7037(96)00193-7

Fellin, M. G., Vance, J., Garver, J. I., & Zattin, M. (2006). The thermal evolution of Corsica as recorded by zircon fission-tracks. *Tectonophysics*, *421*(3-4), 299–317. https://doi.org/10.1016/j.tecto.2006.05.001

Ferrando, S., Bernoulli, D., & Compagnoni, R. (2004). The Canavese zone (internal western Alps), a distal margin of Adria. *Schweizerische Mineralogische und Petrographische Mitteilungen*, *84*, 1–20.

Flowers, R. M., Shuster, D. L., Wernicke, B. P., & Farley, K. A. (2007). Radiation damage control on apatite (U–Th)/He dates from the Grand Canyon region, Colorado Plateau. *Geology*, *35*(5), 447–450. https://doi.org/10.1130/G23471A.1

Foeken, J. P. T., Dunai, T. J., Bertotti, G., & Andriessen, P. A. M. (2003). Late Miocene to present exhumation in the Ligurian Alps (southwest Alps) with evidence for accelerated denudation during the Messinian salinity crisis. *Geology*, *31*(9), 797–800. https://doi.org/10.1130/G19572.1

Foeken, J. P. T., Stuart, F. M., Dobson, K. J., Persano, C., & Vilbert, D. (2006). A diode laser systemfor heating minerals for (U-Th)/He chronometry. *Geochemistry, Geophysics, Geosystems*, *7*, Q04015. https://doi.org/10.1029/2005GC001190

Froitzheim, N., & Manatschal, G. (1996). Kinematics of Jurassic rifting, mantle exhumation, and passive-margin in the Austroalpine and Penninic nappes (eastern Switzerland). *Geological Society of America Bulletin*, *108*(9), 1120–1133. https://doi.org/10.1130/0016-7606(1996)108%3C1120:KOJRME%3E2.3.CO;2

Gaggero, L., Cortesogno, L., & Bertrand, J. M. (2004). The Pre-Namurian basement of the Ligurian Alps: A review of the lithostratigraphy, pre-Alpine metamorphic evolution and regional comparisons. *Periodico di Mineralogia*, *73*, 85–96.

Guenthner, W. R., Reiners, P. W., Ketcham, R. A., Nasdala, L., & Giester, G. (2013). Helium diffusion in natural zircon: Radiation damage, anisotropy and the interpretation of zircon (U-Th)/He Thermochronology. *American Journal of Science*, *313*(3), 145–198. https://doi.org/10.2475/03.2013.01

Handy, M. R., Schmid, S. M., Bousquet, R., Kissling, E., & Bernoulli, D. (2010). Reconciling plate-tectonic reconstructions of Alpine Tethys with the geological-geophysical record of spreading and subduction in the Alps. *Earth-Science Reviews*, *102*, 121–158.

Hart, N. R., Stockli, D. F., Lavier, L. L., & Hayman, N. W. (2017). Thermal evolution of a hyperextended rift basin, Mauleon Basin, western Pyrenees. *Tectonics*, *36*, 1103–1128. https://doi.org/10.1002/2016TC004365

Haupert, I., Manatschal, G., Decarlis, A., & Unternehr, P. (2016). Upper-plate magma-poor rifted margins: Stratigraphic architecture and structural evolution. *Marine and Petroleum Geology*, *69*, 241–261. https://doi.org/10.1016/j.marpetgeo.2015.10.020

Henry, D. J., et al. (2005). The Ti-saturation surface for low-to-medium pressure metapelitic biotites: Implications for geothermometry and Ti-substitution mechanisms. *American Mineralogist*, *90*(2-3), 316–328. https://doi.org/10.2138/am.2005.1498

Hurford, A. J., & Green, P. F. (1983). The zeta calibration of fission track dating. *Chemical Geology*, *41*, 285–317. https://doi.org/10.1016/S0009-2541(83)80026-6

Incerpi, N., Martire, L., Manatschal, G., & Bernasconi, S. M. (2017). Evidence of hydrothermal fluid flow in a hyperextended rifted margin: The case study of the Err Nappe (SE Switzerland). *Swiss Journal of Geosciences*, *110*(2), 439–456. https://doi.org/10.1007/s00015-016-0235-2

Ketcham, R. A. (2005). Forward and inverse modeling of low-temperature thermochronometry data. *Reviews in Mineralogy and Geochemistry*, *58*, 275–314.

Jäger, E. (1967). Die Bedeutung der Biotit Alterswerte. In: Jäger E., Niggli E., Wenk E. (Eds.), Rb/Sr Altersbestimmungen an Glimmern der Zentralalpen. *Beitraege zur Geologischen Karte der Schweiz*, *66*, 28–31.

Ketcham, R. A., Gautheron, C., & Tassan-Got, L. (2011). Accounting for long alpha-particle stopping distances in (U–Th–Sm)/He geochronology: Refinement of the baseline case. *Geochimica et Cosmochimica Acta*, *75*(24), 7779–7791. https://doi.org/10.1016/j.gca.2011.10.011

Lemoine, M., & Trümpy, R. (1987). Pre-oceanic rifting in the Alps. *Tectonophysics*, *133*(3-4), 305–320. https://doi.org/10.1016/0040-1951(87)90272-1

Lemoine, M., Bas, T., Arnaud-Vanneau, A., Arnaud, H., Dumont, T., Gidon, M., … Tricart, P. (1986). The continental margin of the Mesozoic Tethys in the Western Alps. *Marine and Petroleum Geology*, *3*, 179–199.

Liao, W. Z., Lin, A. T., Liu, C. S., Oung, J. N., & Wang, Y. (2014). Heat flow in the rifted continental margin of the South China Sea near Taiwan and its tectonic implications. *Journal of Asian Earth Sciences*, *92*, 233–244. https://doi.org/10.1016/j.jseaes.2014.01.003

Maino, M., Dallagiovanna, G., Dobson, K., Gaggero, L., Persano, C., Seno, S., & Stuart, F. M. (2012). Testing models of orogen exhumation using zircon (U–Th)/He thermochronology: Insights from the Ligurian Alps, Northern Italy. *Tectonophysics*, *560-561*(561), 84–93. https://doi.org/10.1016/j.tecto.2012.06.045

Maino, M., Dallagiovanna, G., Gaggero, L., Seno, S., & Tiepolo, M. (2012). U–Pb zircon geochronological and petrographic constraints on late to post-collisional Variscan magmatism and metamorphism in the Ligurian Alps, Italy. *Geological Journal*, *47*(6), 632–652. https://doi.org/10.1002/gj.2421

Maino, M., Decarlis, A., Felletti, F., & Seno, S. (2013). Tectono-sedimentary evolution of the tertiary Piedmont Basin (NW Italy) within the Oligo–Miocene central Mediterranean geodynamics. *Tectonics*, *32*, 593–619. https://doi.org/10.1002/tect.20047

Maino, M., Casini, L., Ceriani, A., Decarlis, A., Di Giulio, A., Seno, S., … Stuart, F. M. (2015). Dating shallow thrusts with zircon (U-Th)/He thermochronometry-the shear heating connection. *Geology*, *43*(6), 495–498. https://doi.org/10.1130/G36492.1

Manatschal, G. (2004). New models for evolution of magma-poor rifted margins based on a review of data and concepts from West Iberia and the Alps. *International Journal of Earth Sciences*, *93*, 432–466.

Manatschal, G., & Bernoulli, D. (1999). Architecture and tectonic evolution of non-volcanic margins: Present-day Galicia and ancient Adria. *Tectonics*, *18*(6), 1099–1119. https://doi.org/10.1029/1999TC900041

Masini, E., Manatschal, G., & Mohn, G. (2013). The Alpine Tethys rifted margins: Reconciling old and new ideas to understand the stratigraphic architecture of magma-poor rifted margins. *Sedimentology*, *60*(1), 174–196. https://doi.org/10.1111/sed.12017

Messiga, B., Oxilia, M., Piccardo, G. B., & Vanossi, M. (1981). Fasi metamorfiche e deformazioni Alpine nel Brianzonese e nel Pre-Piemontese – Piemontese esterno delle Alpi Liguri: un possible modello evolutivo. *Rendiconti della Societa Italiana di Mineralogia e Petrologia*, *38*(1), 261–280.

Mohn, G., Manatschal, G., Beltrando, M., Masini, E., & Kusznir, N. (2012). Necking of continental crust in magma-poor rifted margins: Evidence from the fossil alpine Tethys margins. *Tectonics*, *31*, TC1012. https://doi.org/10.1029/2011TC002961

Naeser, N. D., Zeitler, P. K., Naeser, C. W., & Cerveny, P. F. (1987). Provenance studies by fission track dating of zircon—Etching and counting procedures. *Nuclear Tracks and Radiation Measurements*, *13*(2-3), 121–126. https://doi.org/10.1016/1359-0189(87)90022-7

Pouchou, J. L., & Pichoir, F. (1988). *Determination of mass absorption coefficients for soft X-rays by use of the electron microprobe* (pp. 319–324). San Francisco: Microbeam Analysis. San Francisco Press.

Reiners, P. W. (2005). Zircon (U-Th)/He thermochronometry. *Reviews in Mineralogy and Geochemistry*, *58*, 151–179.

Reiners, P. W., & Brandon, M. T. (2006). Using thermochronology to understand orogenic erosion. *Annual Review of Earth and Planetary Sciences*, *34*(1), 419–466. https://doi.org/10.1146/annurev.earth.34.031405.125202

Reiners, P. W., Spell, T. L., Nicolescu, S., & Zanetti, K. A. (2004). Zircon (U-Th)/He thermochronometry: He diffusion and comparisons. *Cosmochimica Acta*, *68*(8), 1857–1887. https://doi.org/10.1016/j.gca.2003.10.021

Satır, M., & Friedrichsen, H. (1986). The origin and evolution of the Menderes massif, WTurkey: A rubidium/strontium and oxygen isotope study. *Geologie Rundschau*, *75*(3), 703–714. https://doi.org/10.1007/BF01820642

Seno, S., Dallagiovanna, G., & Vanossi, M. (2005a). A kinematic evolution model for the Penninic sector of the central Ligurian Alps. *International Journal of Earth Sciences*, *94*(1), 114–129. https://doi.org/10.1007/s00531-004-0444-1

Seno, S., Dallagiovanna, G., & Vanossi, M. (2005b). Pre-Piedmont and Piedmont-Ligurian nappes in the central sector of the Ligurian Alps: A possible pathway for their superposition on to the inner Briançonnais units. *Bollettino della Societa Geologica Italiana*, *124*(2), 455–464.

Seymour, N. M., Stockli, D. F., Beltrando, M., & Smye, A. J. (2016). Tracing the thermal evolution of the Corsican lower crust during Tethyan rifting. *Tectonics*, *35*, 2439–2466. https://doi.org/10.1002/2016TC004178

Sutra, E., Manatschal, G., Mohn, G., & Unternehr, P. (2013). Quantification and restoration of extensional deformation along the Western Iberia and Newfoundland rifted margins. *Geochemistry, Geophysics, Geosystems*, *14*(8), 2575–2597. https://doi.org/10.1002/ggge.20135

Tugend, J., Manatschal, G., Kusznir, N. J., & Masini, E. (2014). Characterizing and identifying structural domains at rifted continental margins: Application to the Bay of Biscay margins and its Western Pyrenean fossil remnants. *Geological Society of London*, *413*, 171–203.

Vacherat, A., Mouthereau, F., Pik, R., Bernet, M., Gautheron, C., Masini, E., … Lahfid, A. (2014). Thermal imprint of rift-related processes in orogens as recorded in the Pyrenees. *Earth and Planetary Science Letters*, *408*, 296–306. https://doi.org/10.1016/j.epsl.2014.10.014

Vance, J. (1999). Zircon fission track evidence for a Jurassic (Tethyan) thermal event in the Western Alps. *Memorie di Scienze Geologiche dell'Università di Padova*, *51*, 473–476.

Vanossi, M. (Ed.) (1991). *Guide Geologiche Regionali, Alpi Liguri* (p. 296). Milan: Be-Ma.

Vanossi, M., Cortesogno, L., Galbiati, B., Messiga, B., Piccardo, G., & Vannucci, R. (1986). Geologia delle Alpi Liguri: dati, problemi, ipotesi. *Memorie della Società Geologica Italiana*, *28*, 5–75.

Verschure, R. H., Andriessen, P. A. M., Boelrijk, N. A. I. M., Hebeda, E. H., Maijer, C., Priem, H. N. A., & Verdurmen, E. A. T. (1980). On the thermal stability of Rb-Sr and K-Ar biotite systems: Evidence from coexisting Sveconorwegian (ca 870 ma) and Caledonian (ca 400 Ma) biotites in SW Norway. *Contributions to Mineralogy and Petrology*, *74*(3), 245–252. https://doi.org/10.1007/BF00371694